Sciencexpress Reports

Discovery of a Three-Dimensional Topological Dirac Semimetal, Na_3Bi

Z. K. Liu,[1]* B. Zhou,[2,3]* Y. Zhang,[3] Z. J. Wang,[4] H. M. Weng,[4] D. Prabhakaran,[2] S.-K. Mo,[3] Z. X. Shen,[1] Z. Fang,[4] X. Dai,[4] Z. Hussain,[3] Y. L. Chen[2,3]†

[1]Stanford Institute for Materials and Energy Sciences, SLAC National Accelerator Laboratory, 2575 Sand Hill Road, Menlo Park, CA 94025, USA. [2]Physics Department, Clarendon Laboratory, University of Oxford, Parks Road, OX1 3PU, UK. [3]Advanced Light Source, Lawrence Berkeley National Laboratory, Berkeley, CA 94720, USA. [4]Beijing National Laboratory for Condensed Matter Physics and Institute of Physics, Chinese Academy of Sciences, Beijing 100190, China.

*These authors contributed equally to this work.

†Corresponding author. E-mail: yulin.chen@physics.ox.ac.uk

Three-dimensional (3D) topological Dirac semimetals (TDSs) represent a novel state of quantum matter that can be viewed as "3D graphene". In contrast to two-dimensional (2D) Dirac fermions in graphene or on the surface of 3D topological insulators, TDSs possess 3D Dirac fermions in the bulk. By investigating the electronic structure of Na_3Bi with angle resolved photoemission spectroscopy, we discovered 3D Dirac fermions with linear dispersions along all momentum directions. Furthermore, we demonstrated the robustness of 3D Dirac fermions in Na_3Bi against in situ surface doping. Our results establish Na_3Bi as a model system of 3D TDSs, which can serve as an ideal platform for the systematic study of quantum phase transitions between rich topological quantum states.

The discoveries of graphene and topological insulators (TIs) have inspired enormous efforts in the search for materials with similar electronic and topological properties (*1–4*). Graphene, a single sheet of carbon atoms, hosts 2D Dirac fermions in its electronic structure (*1*, *2*, *5*); TIs are materials with bulk energy gap but gapless surface states formed by an odd number of Dirac fermions with helical spin texture (*3*, *4*, *6–8*). In the course of this search, the following questions arose: Does a 3D counterpart of graphene exist? Can materials other than insulators possess unusual topology in their electronic structures?

In a class of materials called the topological Dirac semimetals both of these questions are answered in the affirmative. There, the bulk conduction and valence bands touch only at discrete (Dirac) points and disperse linearly along all (three) momentum directions, forming bulk (3D) Dirac fermions – a natural 3D counterpart of graphene. Interestingly, although similar electronic structure was discussed more than seven decades ago (*9*), its topological classification was only appreciated recently (*10–15*), leading to the theoretical proposal of topological Dirac semimetals (*12–16*).

The distinct electronic structure of a topological Dirac semimetal not only makes it possible to realize some exciting phenomena and applications of graphene (*17*) in 3D materials, but also gives rise to many unique properties, such as the giant diamagnetism that diverges logarithmically when the Fermi-energy (E_F) is approaching the 3D Dirac point (*16*, *18*, *19*), quantum magnetoresistance showing linear field dependence in the bulk (*20*, *21*), unique Landau level structures under strong magnetic field, and oscillating quantum spin Hall effect in quantum well structures (*15*, *22*). Interestingly, the 3D Dirac fermion in a topological Dirac semimetal is composed of two overlapping Weyl fermions (which are chiral massless particles previously studied extensively in high-energy physics, e.g., as a description of neutrinos) (*23*) that can be separated in the momentum space if time reversal or inversion symmetry is broken. This would result in a topological Weyl semimetal, another novel topological quantum state showing unique Fermi-arcs geometry (*12*, *24*), exhibiting pressure induced anomalous Hall effect (*25*) and quantized anomalous Hall effect in quantum well structures (*24*).

Besides these unusual properties, the topological Dirac semimetal is the neighbor state to various states (Fig. 1A, B) (*12–16*, *26*) ranging from regular band insulators to topological superconductors. This versatility makes the topological Dirac semimetal an ideal mother compound for the realization of other novel states as well as a platform for the systematic study of topological quantum phase transitions.

The physical realization of the topological Dirac semimetal is, however, challenging. In principle, it may be realized through topological phase transitions, such as tuning chemical composition or spin-orbital coupling strength to the quantum critical point through a normal insulator - topological insulator transition (Fig. 1B). Recently, it was realized that the crystal symmetry can protect and stabilize 3D Dirac points in several stoichiometric compounds such as β-cristobalite BiO_2 (*14*) and A_3Bi (A=Na, K, Rb) family of compounds (*15*). Because of the metastable nature of β-cristobalite BiO_2, we chose to study Na_3Bi.

We performed angle resolved photoemission spectroscopy (ARPES) measurements to investigate the electronic structures of Na_3Bi (001) single crystals. Further details of the sample preparation and ARPES experiments are available in (*27*). The crystal structure of Na_3Bi (Fig. 1C) is comprised of stacked …Na - (Na/Bi) - Na… triple-layer groups, with the adjacent triple-layers rotated by 60 degrees with respect to each other. The 3D Brillouin zone (BZ) of Na_3Bi is illustrated in Fig. 1D with high symmetry points indicated. According to recent ab initio calculations (*15*), a pair of 3D Dirac fermions are located near the Γ point in each BZ (labeled as "D" in Fig. 1D), with linear dispersion along k_x, k_y, and k_z directions. Because a 3D Dirac fermion is a surface in four-dimensional space ($E = V_x \cdot k^D{}_x + V_y \cdot k^D{}_y + V_z \cdot k^D{}_z$, where V_x, V_y and V_z are the Fermi-velocities along *x, y*, and *z* directions, respectively; and $k^D{}_x$, $k^D{}_y$ and $k^D{}_z$ represent the momentum measured from the Dirac point), in Fig. 1E, we visualize it by using $k^D{}_x$, $k^D{}_y$ and $k^D{}_z$ as variables and colors as representation of E (the 4th dimension). The projections of the 3D Dirac fermion onto two 2D momentum planes are shown in Fig. 1F, G. The figures reflect the calculated small in-plane and large out-of-plane anisotropy ($V_x \approx V_y = 3.74\times10^5$ m/s, $V_z = 2.89\times10^4$ m/s).

The overall electronic structure from ARPES measurements is summarized in Fig. 2. The characteristic peaks of Na and Bi elements are evident in the core-level spectra (Fig. 2A); the band dispersions (Fig. 2B) agree well with our ab initio calculations, represented by solid lines [details of the calculations can be found in (*27*)]. The electronic structure at the Dirac point is illustrated in Fig. 2C, showing a cone-shape with linear dispersions [details on selecting k_z positions and identifying Dirac

points in momentum space can be found in (*27*)]. This Dirac cone dispersion results in a point-like Fermi-surface (FS) at $\bar{\Gamma}$ in the projected 2D BZ (Fig. 2D). Moreover, the constant energy contours of the Dirac cone at different binding energies (Fig. 2E) demonstrate the small in-plane anisotropy.

To demonstrate the 3D nature of the Dirac cone in Na_3Bi, we need to illustrate that the band dispersion is also linear along k_z (as well as k_x and k_y), which was achieved by performing photon-energy dependent ARPES measurements (*27*, *28*). By assembling the measurements under broad range of photon energies (*27*), we obtained the band structures of Na_3Bi throughout the 3D BZ. Figure 3A illustrates the complete FS of Na_3Bi in a 3D BZ, showing a pair of point-like FSs in the vicinity of Γ at $k_x = k_y = 0$ and $k_{z\pm} = \pm 0.095$ /Å or $\pm 0.29\ \pi/c$, where c is the z-direction lattice constant, which agrees well with our ab initio calculations that predict two Dirac points at $k_{z\pm} = \pm 0.26\pi/c$ (*15*). Note that in Fig. 3A(ii), which shows the data for a Na-deficient sample surface, an additional cylindrical FS appears and vertically crosses the whole 3D BZ (and thus is dispersionless along k_z). This feature originates from the surface states (*27*, *28*) that emerge due to the loss of the surface Na atoms, which easily migrate away during the experiment (*27*).

Besides the 3D FS, we can investigate the band dispersion along all three k-directions. Similar to Fig. 2C, the 3D electronic structure along k^D_y-k^D_z direction is illustrated in Fig. 3B, showing a clearly elongated (along k^D_z direction) Dirac cone (corresponding to a much smaller V_z - see Fig. 3B, C). Furthermore, we can study the detailed dispersions along each momentum direction (see schematics in Fig. 3D-F): for a 3D Dirac fermion, ARPES measurements along any k-direction should yield either linear or hyperbolic dispersions depending on whether the measurement cuts through the Dirac point – this is different from the usual parabolic dispersions of massive electrons.

In Fig. 3D-F (i-iv), we use four examples along each k-direction to show typical ARPES dispersions on Na_3Bi [for more measurements and analysis see (*27*)]. Along each k-direction, the dispersion evolves from linear [Fig. 3D-F (i)] to hyperbolic [Fig. 3D-F (ii~iv)] shape, as expected. Notably, to fit all of the ARPES measurements [including those in (*27*)], we only need one set of 3D Dirac cone parameters (V_x = 2.75 eV•Å or 4.17×10^5 m/s, V_y = 2.39 eV•Å or 3.63×10^5 m/s, and V_z = 0.6 eV•Å or 0.95×10^5 m/s). This excellent agreement proves that the bulk band structure of Na_3Bi forms 3D Dirac cones, with a large anisotropy along the k_z direction ($V_z \approx 0.25V_x$, see Fig. 3C).

To test the robustness of 3D Dirac fermion in Na3Bi, we deliberately modified the sample surface (by in situ evaporating K-atoms, see Fig. 4A, B) and monitored the band dispersions' evolution with the increase of surface impurities. In addition, the K-doping can compensate the charge loss caused by the surface Na-atom loss discussed above [and in (*27*)]. In fact, we were even able to over-compensate the charge loss with sufficient doping and observed the upper part of Dirac cone beyond the Dirac point (Fig. 4C). With the increase of K-doping, the E_F shifts upward (Fig. 4D-F), whereas the surface state band disappears (Fig. 4E, F) owing to the deterioration of the sample surface by randomly deposited K-atoms. On the other hand, the bulk Dirac cone (both the linear dispersion and the Dirac point) persists despite such surface deterioration (Fig. 4E, F), supporting the notion that the Dirac fermion is protected by the bulk crystal symmetry (which is preserved during surface K-doping).

The topological Dirac semimetal Na_3Bi realizes a 3D counterpart of graphene, opening the door for the exploration of other 3D TDSs, some of which may realize various exciting applications of graphene in 3D materials. Furthermore, the extremely long Fermi-wavelength (which diverges at the Dirac points) of the bulk conducting electrons in a topological Dirac semimetal can greatly enhance the Ruderman-Kittel-Kasuya-Yosida interaction, making it possible to realize ferromagnetic states by unusually dilute magnetic doping [similar to the Dirac surface states in a topological insulator (*29*)] – which could make the topological Dirac semimetal an ideal platform for spintronics applications.

References and Notes

1. A. K. Geim, K. S. Novoselov, The rise of graphene. *Nat. Mater.* **6**, 183–191 (2007). Medline doi:10.1038/nmat1849
2. A. H. Castro Neto, F. Guinea, N. M. R. Peres, K. S. Novoselov, A. K. Geim, The electronic properties of graphene. *Rev. Mod. Phys.* **81**, 109–162 (2009). doi:10.1103/RevModPhys.81.109
3. M. Z. Hasan, C. L. Kane, *Colloquium*: Topological insulators. *Rev. Mod. Phys.* **82**, 3045–3067 (2010). doi:10.1103/RevModPhys.82.3045
4. X.-L. Qi, S.-C. Zhang, Topological insulators and superconductors. *Rev. Mod. Phys.* **83**, 1057–1110 (2011). doi:10.1103/RevModPhys.83.1057
5. K. S. Novoselov, A. K. Geim, S. V. Morozov, D. Jiang, Y. Zhang, S. V. Dubonos, I. V. Grigorieva, A. A. Firsov, Electric field effect in atomically thin carbon films. *Science* **306**, 666–669 (2004). Medline doi:10.1126/science.1102896
6. C. L. Kane, E. J. Mele, Quantum spin Hall effect in graphene. *Phys. Rev. Lett.* **95**, 226801 (2005). Medline doi:10.1103/PhysRevLett.95.226801
7. L. Fu, C. L. Kane, E. J. Mele, Topological insulators in three dimensions. *Phys. Rev. Lett.* **98**, 106803 (2007). Medline doi:10.1103/PhysRevLett.98.106803
8. J. E. Moore, The birth of topological insulators. *Nature* **464**, 194–198 (2010). Medline doi:10.1038/nature08916
9. C. Herring, Accidental Degeneracy in the Energy Bands of Crystals. *Phys. Rev.* **52**, 365–373 (1937). doi:10.1103/PhysRev.52.365
10. S. Murakami, Phase transition between the quantum spin Hall and insulator phases in 3D: Emergence of a topological gapless phase. *New J. Phys.* **9**, 356 (2007). doi:10.1088/1367-2630/9/9/356
11. G. E. Volovik, "Quantum phase transitions from topology in momentum space," in *Quantum Analogues: From Phase Transitions to Black Holes and Cosmology*, W. Unruh, R. Schützhold, Eds. Lecture Notes in Physics (Springer, Berlin, Heidelberg, 2007), vol. 718, pp. 31–73.
12. X. Wan, A. M. Turner, A. Vishwanath, S. Y. Savrasov, Topological semimetal and Fermi-arc surface states in the electronic structure of pyrochlore iridates. *Phys. Rev. B* **83**, 205101 (2011). doi:10.1103/PhysRevB.83.205101
13. A. A. Burkov, L. Balents, Weyl semimetal in a topological insulator multilayer. *Phys. Rev. Lett.* **107**, 127205 (2011). Medline doi:10.1103/PhysRevLett.107.127205
14. S. M. Young, S. Zaheer, J. C. Teo, C. L. Kane, E. J. Mele, A. M. Rappe, Dirac semimetal in three dimensions. *Phys. Rev. Lett.* **108**, 140405 (2012). Medline doi:10.1103/PhysRevLett.108.140405
15. Z. Wang, Y. Sun, X.-Q. Chen, C. Franchini, G. Xu, H. Weng, X. Dai, Z. Fang, Dirac semimetal and topological phase transitions in A_3Bi (A=Na, K, Rb). *Phys. Rev. B* **85**, 195320 (2012). doi:10.1103/PhysRevB.85.195320
16. P. Goswami, S. Chakravarty, Quantum criticality between topological and band insulators in 3+1 dimensions. *Phys. Rev. Lett.* **107**, 196803 (2011). Medline doi:10.1103/PhysRevLett.107.196803
17. A. K. Geim, Graphene: Status and prospects. *Science* **324**, 1530–1534 (2009). Medline doi:10.1126/science.1158877
18. M. Koshino, T. Ando, Anomalous orbital magnetism in Dirac-electron systems: Role of pseudospin paramagnetism. *Phys. Rev. B* **81**, 195431 (2010). doi:10.1103/PhysRevB.81.195431
19. E. Röber, K. Hackstein, H. Coufal, S. Sotier, Magnetic susceptibility of liquid $Na_{1-x}Bi_x$ Alloys. *Phys. Status Solidi B* **93**, K99–K102 (1979). doi:10.1002/pssb.2220930244
20. A. A. Abrikosov, Quantum magnetoresistance. *Phys. Rev. B* **58**, 2788–2794 (1998). doi:10.1103/PhysRevB.58.2788
21. W. Zhang, R. Yu, W. Feng, Y. Yao, H. Weng, X. Dai, Z. Fang, Topological aspect and quantum magnetoresistance of β-Ag_2Te. *Phys. Rev. Lett.* **106**, 156808 (2011). Medline doi:10.1103/PhysRevLett.106.156808
22. C.-X. Liu, H. J. Zhang, B. Yan, X.-L. Qi, T. Frauenheim, X. Dai, Z. Fang, S.-C. Zhang, Oscillatory crossover from two-dimensional to three-dimensional topological insulators. *Phys. Rev. B* **81**, 041307 (2010). doi:10.1103/PhysRevB.81.041307
23. G. E. Volovik, *The Universe in a Helium Droplet* (Clarendon, Oxford, 2003).
24. G. Xu, H. Weng, Z. Wang, X. Dai, Z. Fang, Chern semimetal and the

quantized anomalous Hall effect in $HgCr_2Se_4$. *Phys. Rev. Lett.* **107**, 186806 (2011). Medline doi:10.1103/PhysRevLett.107.186806
25. K.-Y. Yang, Y.-M. Lu, Y. Ran, Quantum Hall effects in a Weyl semimetal: Possible application in pyrochlore iridates. *Phys. Rev. B* **84**, 075129 (2011). doi:10.1103/PhysRevB.84.075129
26. F. R. Klinkhamer, G. E. Volovik, Emergent CPT violation from the splitting of Fermi points. *Int. J. Mod. Phys. A* **20**, 2795–2812 (2005). doi:10.1142/S0217751X05020902
27. Materials and methods are available as supporting materials on *Science* Online.
28. Y. Chen, Studies on the electronic structures of three-dimensional topological insulators by angle resolved photoemission spectroscopy. *Front. Phys* **7**, 175–192 (2012). doi:10.1007/s11467-011-0197-9
29. Q. Liu, C.-X. Liu, C. Xu, X.-L. Qi, S.-C. Zhang, Magnetic impurities on the surface of a topological insulator. *Phys. Rev. Lett.* **102**, 156603 (2009). Medline doi:10.1103/PhysRevLett.102.156603
30. P. E. Blöchl, Projector augmented-wave method. *Phys. Rev. B* **50**, 17953–17979 (1994). Medline doi:10.1103/PhysRevB.50.17953
31. G. Kresse, D. Joubert, From ultrasoft pseudopotentials to the projector augmented-wave method. *Phys. Rev. B* **59**, 1758–1775 (1999). doi:10.1103/PhysRevB.59.1758
32. G. Kresse, J. Furthmüller, Efficient iterative schemes for ab initio total-energy calculations using a plane-wave basis set. *Phys. Rev. B* **54**, 11169–11186 (1996). Medline doi:10.1103/PhysRevB.54.11169
33. J. P. Perdew, K. Burke, M. Ernzerhof, Generalized gradient approximation made simple. *Phys. Rev. Lett.* **77**, 3865–3868 (1996). Medline doi:10.1103/PhysRevLett.77.3865
34. A. Damascelli, Z. Hussain, Z.-X. Shen, Angle-resolved photoemission studies of the cuprate superconductors. *Rev. Mod. Phys.* **75**, 473–541 (2003). doi:10.1103/RevModPhys.75.473
35. A. Damascelli, Probing the electronic structure of complex systems by ARPES. *Phys. Scr.* **2004**, 61 (2004). doi:10.1238/Physica.Topical.109a00061
36. S. Hüfner, Photoelectron Spectroscopy: Principles and Applications (Springer, Berlin, ed. 3, 2003).
37. A. Samsavar, T. Miller, T.-C. Chiang, Photoemission study of the final band in Ag(111). *J. Phys. Condens. Matter* **2**, 1141–1148 (1990). doi:10.1088/0953-8984/2/5/008
38. V. N. Strocov, Intrinsic accuracy in 3-dimensional photoemission band mapping. *J. Electron Spectrosc. Relat. Phenom.* **130**, 65–78 (2003). doi:10.1016/S0368-2048(03)00054-9

Acknowledgements: We thank X. L. Qi and Z. Wang for insightful discussions, and P. Han and R. Yang for the help in data analysis. Y. L. C and B. Z acknowledge the support from the EPSRC (UK) grant EP/K04074X/1 and a DARPA (US) MESO project (no. N66001-11-1-4105). Z. K. L and Z. X. S acknowledge the support from the Department of Energy under contract DE-AC02-76SF00515. Z.F, X.D and H.M.W acknowledge the supports by the NSF of China, the National Basic Research Program of China, and the International Science and Technology Cooperation Program of China. The experiments were performed, and data were collected at Beamline 10.0.1 of the Advanced Light Source, Lawrence Berkeley National Lab, USA.

Supplementary Materials
www.sciencemag.org/cgi/content/full/science.1245085/DC1
Materials and Methods
Figs. S1 to S8
References (*30–38*)

23 August 2013; accepted 02 January 2014
Published online 16 January 2014
10.1126/science.1245085

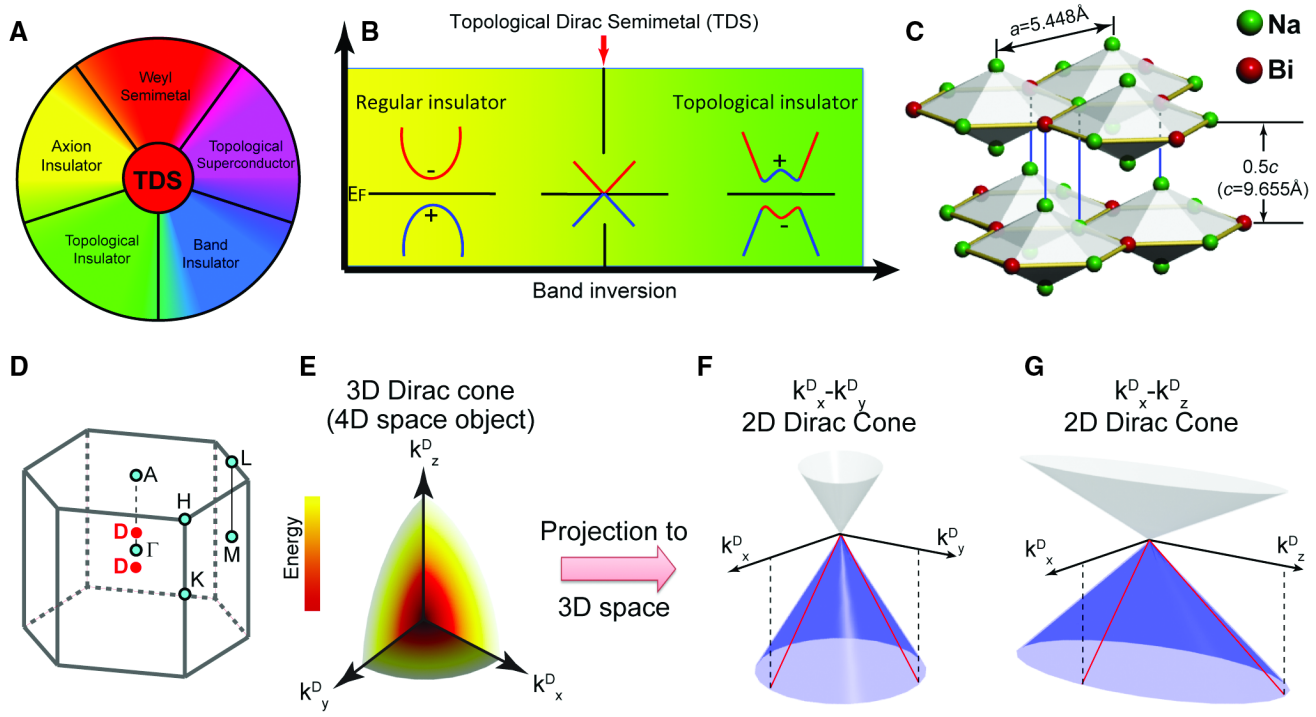

Fig. 1. Basic characteristics of the TDS. (**A**) The TDS state neighbors various novel states. (**B**) The TDS state may be realized at the quantum critical point in the topological quantum phase transition from a normal insulator to a topological insulator. The "+" and "–" signs denote the even and odd parity of the bands at the time reversal invariant point, respectively. (**C**) Crystal structure and (**D**) the BZof Na_3Bi. Cyan dots indicate the high symmetry points of the BZ; and the red dots highlight the 3D Dirac point positions. (**E**) Visualization of a 3D Dirac fermion dispersion $\left(E = V_x \cdot k^D{}_x + V_y \cdot k^D{}_y + V_z \cdot k^D{}_z\right)$, color scale is used to represent energy. (**F**, **G**) Projection of the 3D Dirac fermion onto (k^D_x, k^D_y, E) and (k^D_x, k^D_z, E) spaces (see text). Red lines outline the linear dispersions along k^D_x, k^D_y and k^D_z directions.

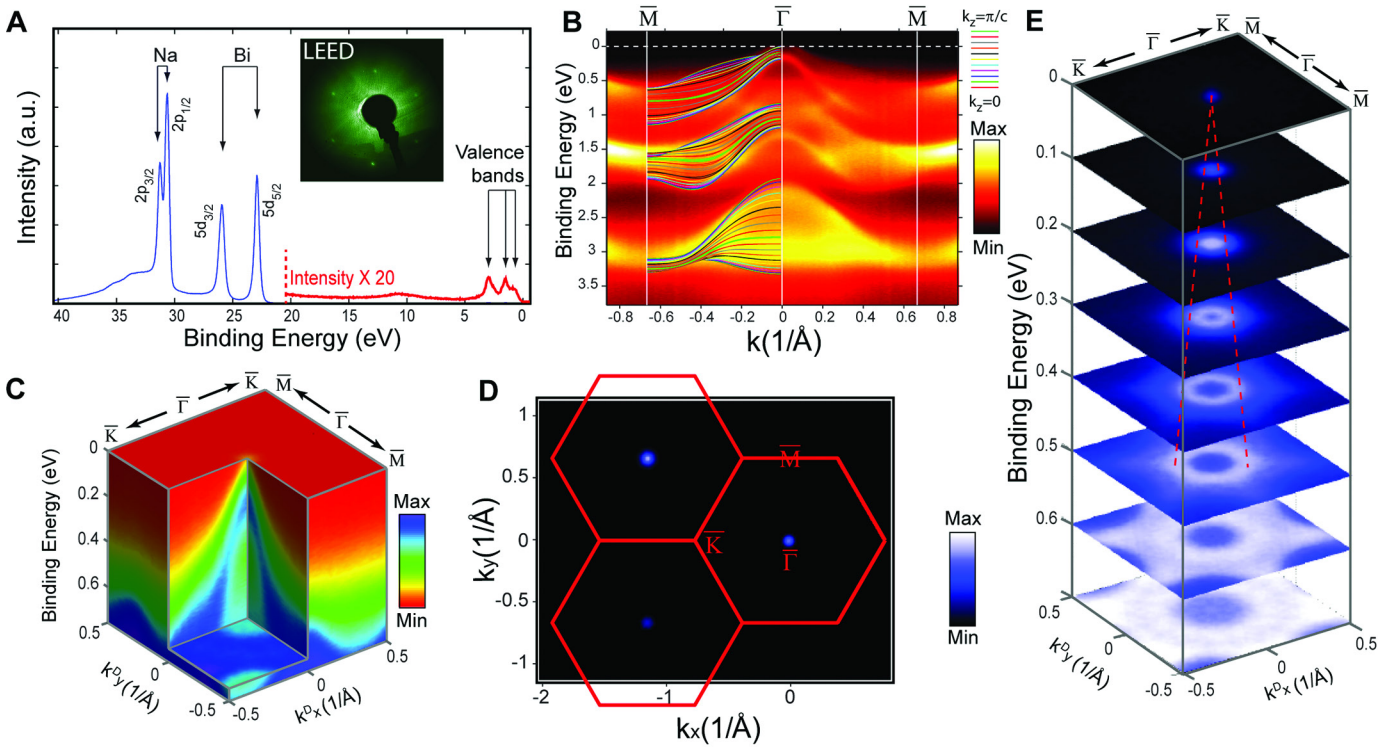

Fig. 2. Electronic structure of Na_3Bi. (**A**) Core level photoemission spectrum clearly shows strong characteristic Na *2p* and Bi *5d* doublet peaks (blue curve). Features at low binding energy (E_B< 21eV) were magnified 20 times to enhance the details (red curve). Inset is the LEED pattern that clearly shows the hexagonal structure of Na_3Bi (001) surface. (**B**) Comparison of the valence band spectra between ARPES measurement (background) and ab initio calculations (solid lines) along the $\bar{M}-\bar{\Gamma}-\bar{M}$ direction. The color of the lines represents different k_z dispersions in the calculation. (**C**) 3D intensity plot of the photoemission spectra at the Dirac point, showing cone-shape dispersion. (**D**) Broad FS map from ARPES measurements that covers three BZs. The red hexagons represent the surface BZ; and the uneven intensity of the FS points of different BZ results from the matrix element effect. (**E**) Stacking plot of constant energy contours at different binding energy shows Dirac cone band structure. Red dotted lines are the guides to the eye that indicate the dispersions and intersect at the Dirac point.

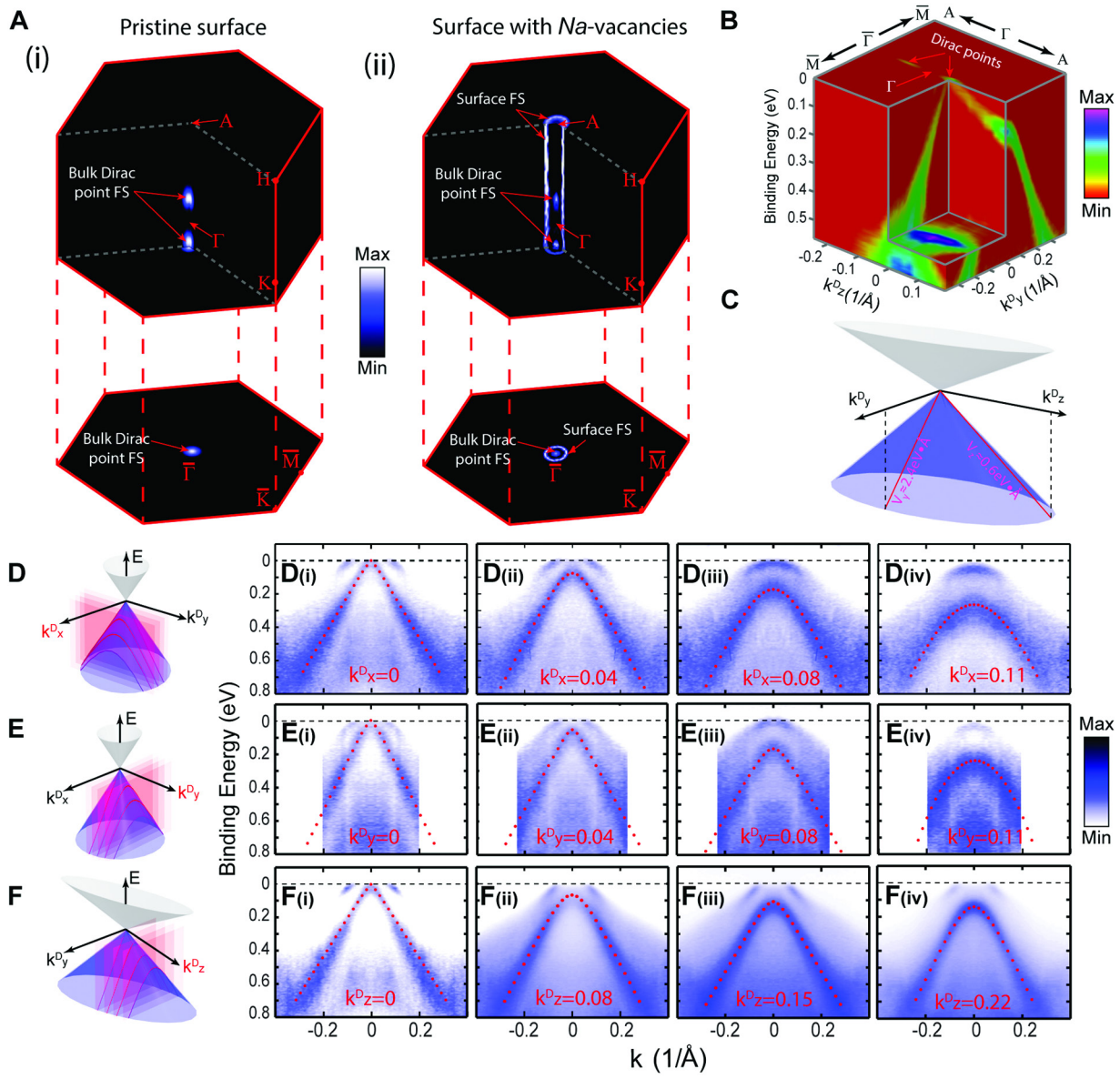

Fig. 3. Dispersion of the 3D Dirac fermion along all three momentum directions. (**A**) FS map across the whole 3D BZ (top panel) and its projection to the surface BZ (bottom panel) on pristine (i) and Na-deficient (ii) surfaces. An additional FS appears in panel (ii) [see text and (*27*) for details]. (**B**) 3D intensity plot of the photoemission spectra (along the k^D_y-k^D_z direction) shows the elongated (along the k^D_z-direction) cone-shape dispersion, indicating the large anisotropy between k_y and k_z direction. (**C**) The schematic of the k^D_y-k^D_z Dirac cone reconstructed from the experimental fit parameters: V_y = 2.4 eV•Å, and V_z = 0.6 eV•Å (*27*). (**D-F**) Schematics show the dispersions (red curves) that slice through the 3D Dirac cones at different (k^D_x, k^D_y or k^D_z) momentum locations, showing either linear or hyperbolic shape. The Dirac velocity parameters obtained from our experiments are: V_x = 2.8 eV•Å, V_y = 2.4 eV•Å, and V_z = 0.6 eV•Å (*27*). **D**(i-iv) Measured dispersion at k^D_x = 0, 0.04, 0.08 and 0.11 Å^{-1}, respectively. Red dotted lines show the fitted dispersions that agree well with the experiments [see text and (27)]. **E**(i-iv) Experiment and fitted dispersions at k^D_y=0, 0.04, 0.08 and 0.11Å^{-1}, respectively. **F**(i-iv) Experiment and fitted dispersions at k^D_z=0, 0.08, 0.15 and 0.22 Å^{-1}, respectively.

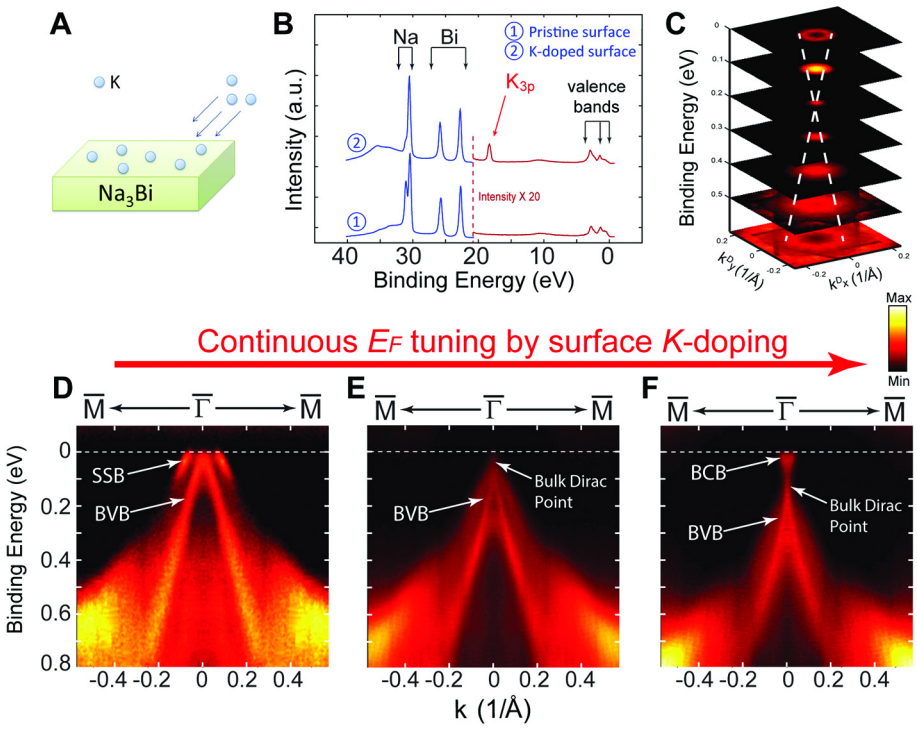

Fig. 4. Bulk Dirac fermion stability and E_F tuning by surface doping. (**A**) Illustration of the in situ surface K-doping. (**B**) Core level photoemission spectra before and after the K-doping show the rise of the K_{3p} core level peak (which can be used to monitor the dosage level). (**C**) Stacking plot of constant energy contours shows the upper Dirac cone after the in situ K-doping. White dashed lines are the guides to the eye that trace the Dirac dispersions. (**D-F**) ARPES intensity plots show the rising of the E_F position with *K*-dosage. Acronyms: SSB, surface state band; BCB, bulk conduction band; BVB, bulk valence band. (D): Before in situ K-doping; (E) at K-doping needed to bring E_F to the bulk Dirac point; (F): further K-doping drives the system into n-type. Note that the SSB in (D) is destroyed by the K-doping, and thus does not show in (E) and (F).